

# Materials Advances

Accepted Manuscript

This article can be cited before page numbers have been issued, to do this please use: G. Skentzos, E. Pramatioti, N. Zink Lorre, A. M. Gutiérrez, E. Nikoli, R. Canton-Vitoria, A. Avramopoulos, N. Tagmatarchis, F. Fernandez-Lazaro and S. Couris, *Mater. Adv.*, 2026, DOI: 10.1039/D5MA01344E.



This is an Accepted Manuscript, which has been through the Royal Society of Chemistry peer review process and has been accepted for publication.

Accepted Manuscripts are published online shortly after acceptance, before technical editing, formatting and proof reading. Using this free service, authors can make their results available to the community, in citable form, before we publish the edited article. We will replace this Accepted Manuscript with the edited and formatted Advance Article as soon as it is available.

You can find more information about Accepted Manuscripts in the [Information for Authors](#).

Please note that technical editing may introduce minor changes to the text and/or graphics, which may alter content. The journal's standard [Terms & Conditions](#) and the [Ethical guidelines](#) still apply. In no event shall the Royal Society of Chemistry be held responsible for any errors or omissions in this Accepted Manuscript or any consequences arising from the use of any information it contains.

Open Access Article. Published on 16 December 2025. Downloaded on 12/24/2025 6:04:46 PM.  
This article is licensed under a Creative Commons Attribution 3.0 Unported Licence.



Materials Advances Accepted Manuscript

1   **Functionalization tuning of the nonlinear optical response of perylene diimide**  
2   **derivatives**

3  
4   George Skentzos,<sup>1</sup> Efrosyni Pramatioti,<sup>1</sup> Nathalie Zink-Lorre,<sup>3</sup> Ana María Gutiérrez-  
5   Vílchez,<sup>3</sup> Eleni Nikoli,<sup>4</sup> Ruben Canton-Vitoria,<sup>4</sup> Aggelos Avramopoulos,<sup>5\*</sup> Nikos  
6   Tagmatarchis,<sup>4\*</sup> Fernando Fernández-Lázaro,<sup>3\*</sup> Stelios Couris<sup>1,2\*</sup>

7  
8   <sup>1</sup> Department of Physics, University of Patras, 26504 Patras, Greece.  
9   <sup>2</sup> Institute of Chemical Engineering Sciences (ICE-HT), Foundation for Research and  
10   Technology-Hellas (FORTH), Patras, 26504, Patras, Greece  
11   <sup>3</sup> Área de Química Orgánica, Instituto de Bioingeniería, Universidad Miguel Hernández de  
12   Elche, Avda. de la Universidad s/n, Elche 03202, Spain.  
13   <sup>4</sup> Theoretical and Physical Chemistry Institute, National Hellenic Research Foundation, 48  
14   Vassileos Constantinou Avenue, Athens 11635, Greece.  
15   <sup>5</sup> Laboratory of Condensed Matter Physics, Department of Physics, University of Thessaly,  
16   3<sup>rd</sup> Old National Road Lamia-Athens, Lamia, 35131, Greece.

17  
18   **ABSTRACT**

19   The synthesis and characterization of perylene diimide (PDI) derivatives functionalized by  
20   electron donating groups at their bay and imide positions has been reported. Five different  
21   PDI derivatives were synthesized and their linear optical and third order non-linear optical  
22   (NLO) properties were studied. The NLO measurements of the synthesized PDI derivatives  
23   were conducted under nanosecond (ns) and femtosecond (fs) laser excitation conditions,  
24   using the Z-scan technique employing 4 ns, 1064/532 nm and 70 fs, 800/400 nm laser pulses.  
25   A noticeable tune of the NLO character between the synthesized PDI derivatives was  
26   observed, revealing the importance of the functionalization of the PDI core by the anchored  
27   electron donating units. The largest NLO value was achieved by the incorporation of *p*-  
28   aminoazobenzene at the PDI bay position. The experimental NLO findings and trends were

further corroborated with theoretical computations of UV-Vis spectra and NLO response, performed using Density Functional Theory (DFT). It was found that both experiment and simulation satisfactorily convey changes of the NLO response, between the studied PDI derivatives. The mechanism which could lead to an efficient tune of the PDIs NLO response, is associated with the modification of their electronic character resulting by the proper PDI core functionalization.

## Introduction

Perylene diimide (PDI) derivatives represent a versatile family of dyes, renowned for their synthetic adaptability and easily modifiable electronic character.<sup>1,2</sup> Indeed, these derivatives have emerged as highly promising molecular materials in organic optoelectronic applications, owing to their tunability and exceptional photophysical properties.<sup>3-6</sup> A plethora of PDI derivatives have been deployed for electronics and light-harvesting applications owing to their exceptional stability, strong fluorescence and broad absorption.<sup>7-10</sup> Their large two-photon absorption (TPA) cross section<sup>11</sup> makes them ideal as excellent NLO materials as well.<sup>12,13</sup> Conversely, azobenzenes, belonging to the wider class of diazenes, are  $\pi$ -conjugated compounds composed of two phenyl rings linked by a nitrogen-nitrogen double bond (N=N), with easily, precisely and facilely adjusted properties via derivatization and incorporation of various functional groups at the phenyl rings.<sup>14</sup> For example, different substituents at the phenyl ring of azobenzenes alter the absorption profile, which can be shifted from the UV-Vis to the NIR region of the electromagnetic spectrum. The incorporation of electron donating amine groups at the *para*-position of the phenyl ring, such as for example in azoanilines, red-shifts the absorption in comparison with the unsubstituted azobenzene, while, on the other hand, extension of the  $\pi$ -conjugation skeleton enhances the TPA properties.<sup>15</sup> Notably, azobenzenes have been employed as ligands for chromophores, such as triarylamine<sup>16</sup> and pyrene,<sup>17</sup> among others, enabling the tuning of the NLO properties.

With the aforementioned in mind and the rich chemistry of PDIs, that enables their seamless combination with target components, incorporation of azobenzenes in the structure of PDIs is of great and significant importance. PDI derivatives, among other organic materials,<sup>18,19</sup> have been shown to be promising organic materials for NLO applications,<sup>13</sup> because of their planar  $\pi$ -aromatic character, their strong electron withdrawing ability (n-type character) and



their strong intramolecular charge transfer ability. Moreover, it has been also proved that modification of their ortho, or bay positions can significantly modify their optical and electronic properties, while substitution at the imide position leads to negligible changes due to the existence of nodes at the nitrogen atoms in both HOMO and LUMO orbitals, which electronically decouple the aromatic core from the imide substituents.<sup>1,20,21</sup>

While the NLO performance of PDI derivatives has been well documented,<sup>7,22-25</sup> the combination of the NLO properties of PDI with those of azobenzene and the investigation of the electronic modifications by targeting different functionalization positions of the perylene framework has yet to be realized. The present study aims to provide new knowledge about these aspects, by combining experimental measurements and theoretical calculations, on how functionalization of some newly synthesized PDIs with electron donating units, like azobenzene, tunes their optical characteristics and their third-order non-linear optical properties.

## Results and discussion

### A. Synthesis and characterization of PDI derivatives A-E

To start with, five different PDI derivatives **A-E** were targeted (**Figure 1**). Azobenzene functionalization of PDI at the imide position, resulting in PDI derivative **A**, allows the study of the NLO properties of a system composed of two electronically decoupled moieties (*vide supra*). Functionalization at the bay position of PDI with azobenzene species, additionally enhances aromatic conjugation in PDI derivative **B**, which may lead to increased TPA absorption.<sup>15</sup> The presence of the ether function allows preserving a certain degree of coplanarity between the PDI core and the azobenzene (*vide infra*), while a C-C direct linkage of PDI and azobenzene would lead to an orthogonal disposition of both moieties, thus disrupting the electronic communication between subunits. Both of these modifications are highly advantageous for various NLO applications. Furthermore, other moieties that extend the aromatic conjugation of perylene, such as a phenyl group at the imide position, yielding PDI derivative **C**, or at the bay position, furnishing PDI derivative **D**, as well as incorporating electron-donating amine yielding PDI derivative **E**, have also been targeted. Consequently, the overall effects on the NLO properties of PDI and azobenzene can be effectively differentiated, based on (a) the type of the electron-donating groups, (b) the degree of aromatic conjugation, and (c) the PDI functionalization position.



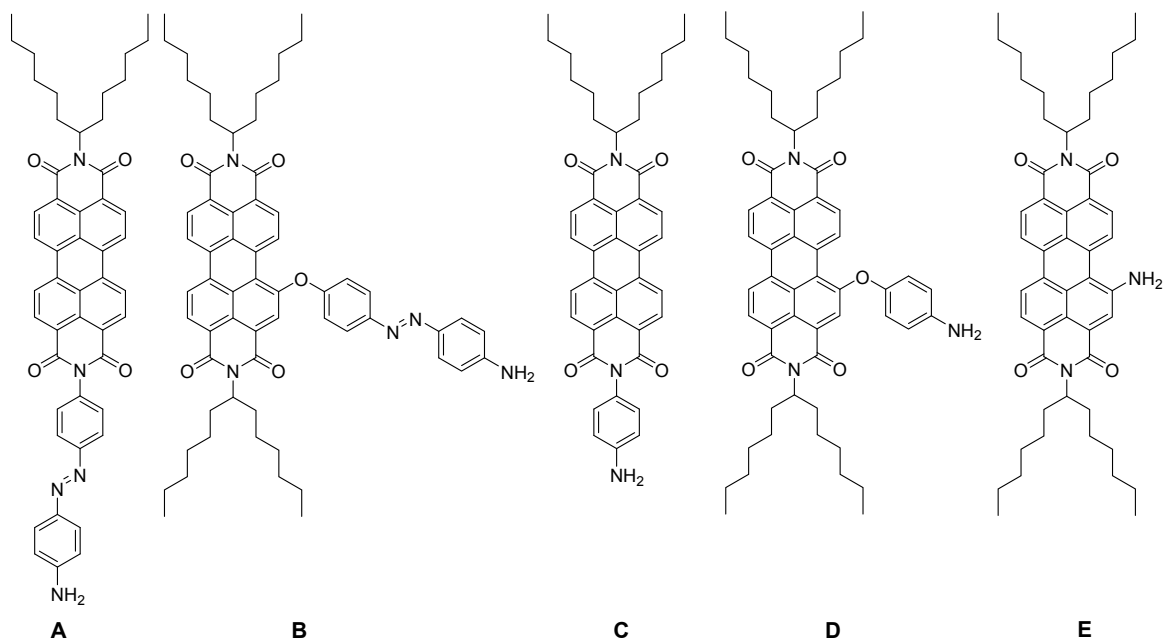
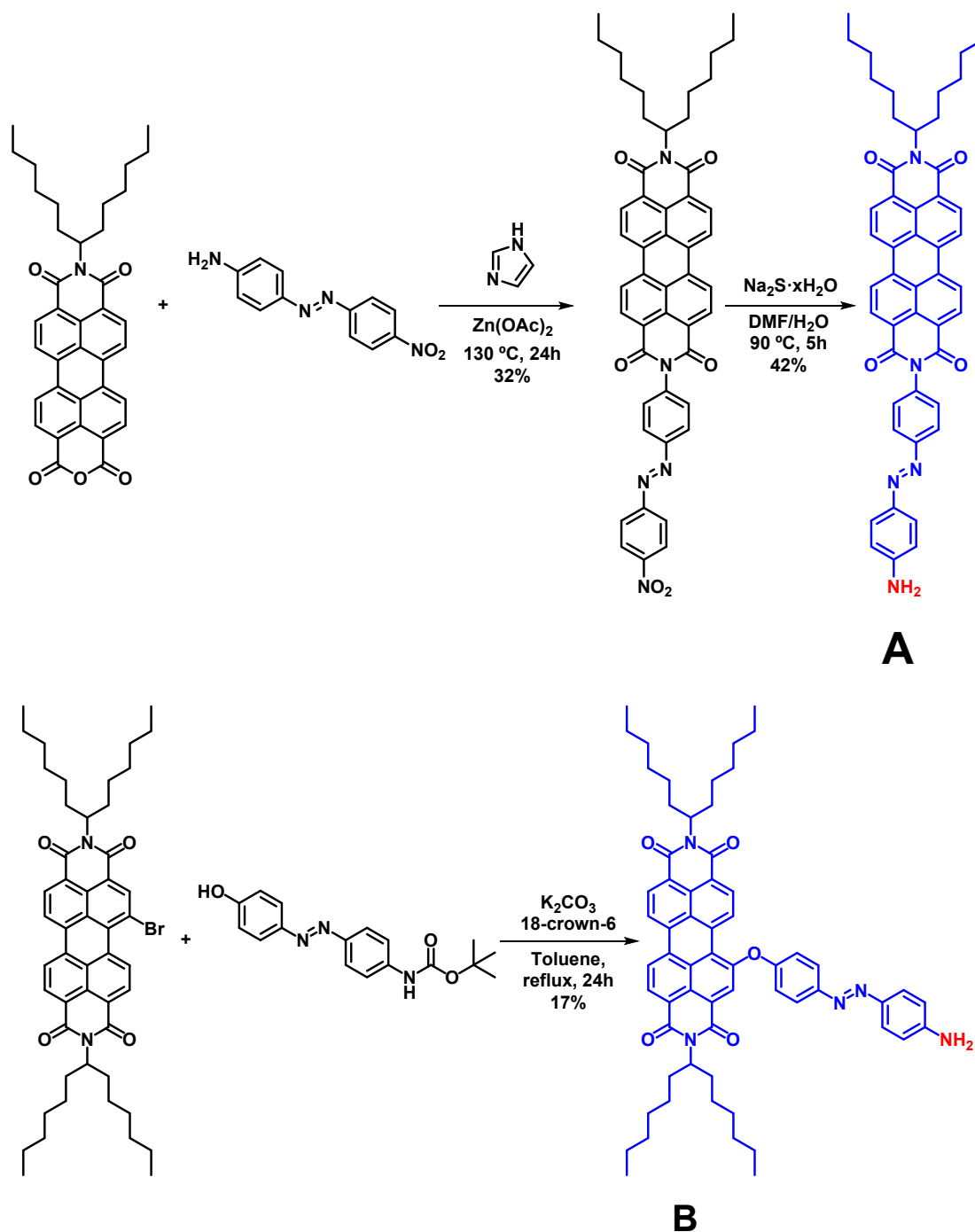


**Figure 1.** Illustrative structure of PDI derivatives **A-E**.

The synthesis of compounds **A** and **B** is illustrated in **Scheme 1**. Briefly, condensation of 4-[(4-nitrophenyl)diazenyl]aniline<sup>26</sup> with *N*-(hexylheptyl)perylene-3,4-dicarboxyanhydride-9,10-dicarboxyimide, in the presence of imidazole, affords the intermediate diimide in 32% yield, which was subsequently reduced with sodium sulfide to afford PDI derivative **A** in 42% yield. On the other hand, PDI derivative **B** was obtained from *N,N'*-di(hexylheptyl)-1-bromoperylene-3,4:9,10-tetracarboxydiimide<sup>27</sup> and the corresponding Boc-protected aminoazophenol in 17% yield. Interestingly, the Boc protective group was spontaneously removed during the purification process, resulting in the direct formation of the final compound. Full experimental details for the synthesis of PDI derivatives **A** and **B** are given at the electronic supplementary material, together with the <sup>1</sup>H- and <sup>13</sup>C-NMR spectra and HR-mass spectrometry data (**Figures S1-S9**). The synthesis of PDI derivatives **C**, **D** and **E** was conducted following literature procedures.<sup>28-30</sup>





**Scheme 1.** Illustrative synthesis of PDI derivatives **A** and **B**.

## **B. Experimental investigation of the NLO response of PDI derivatives A-E**

The NLO response of PDI derivatives **A-E** was studied under nanosecond (ns) and femtosecond (fs) laser excitation conditions, using the Z-scan technique,<sup>31,32</sup> employing 4 ns,



1064/532 nm and 70 fs, 800/400 nm laser pulses, respectively. The details concerning the Z-scan technique and the laser sources used are given in the ESI.

### UV-Vis absorption spectra of PDI derivatives A-E

The UV-Vis absorption spectra of PDI derivatives A-E were studied both experimentally and theoretically. For this, the electronic absorption spectra of different concentration of PDIs A-E were measured and compared with the calculated ones.

*Experimental Investigation:* In **Figure 2**, some representative UV-Vis absorption spectra of the PDI derivatives A-E dissolved in DMF are depicted (for comparison purposes, all having the same concentration of 0.25 mg/mL). As can be seen, the absorption spectrum of PDI A is dominated by three strong absorptions, located at 527, 491 and 460 nm (corresponding to the (0,0), (0,1), and (0,2) electronic transitions, respectively) and a broad absorption band at 404 nm; a similar structure is observed in the UV-Vis spectra of PDI derivatives B-D, with the position and the broadening of each absorption band depending on the nature of the substituent and/or the position of anchoring. For example, substitution with electron donating groups at the bay area of PDI, results in red-shifting of the absorption bands due to electronic interactions between the perylene skeleton and the electron donating moieties (compare e.g. derivative A vs B, and C vs D).<sup>33</sup> So, in the case of B, these bands are red-shifted compared to those of A, appearing at 531, 501, 463 and 408 nm, respectively; in the case of C, the corresponding bands are observed at 525, 489 and 459 nm, while for D they appear at 546, 510 and 477 nm (weak shoulder), respectively. Lastly, PDI derivative E exhibits two broad absorption bands at 607 and 423 nm, and two weaker absorptions at 403 and 388 nm.



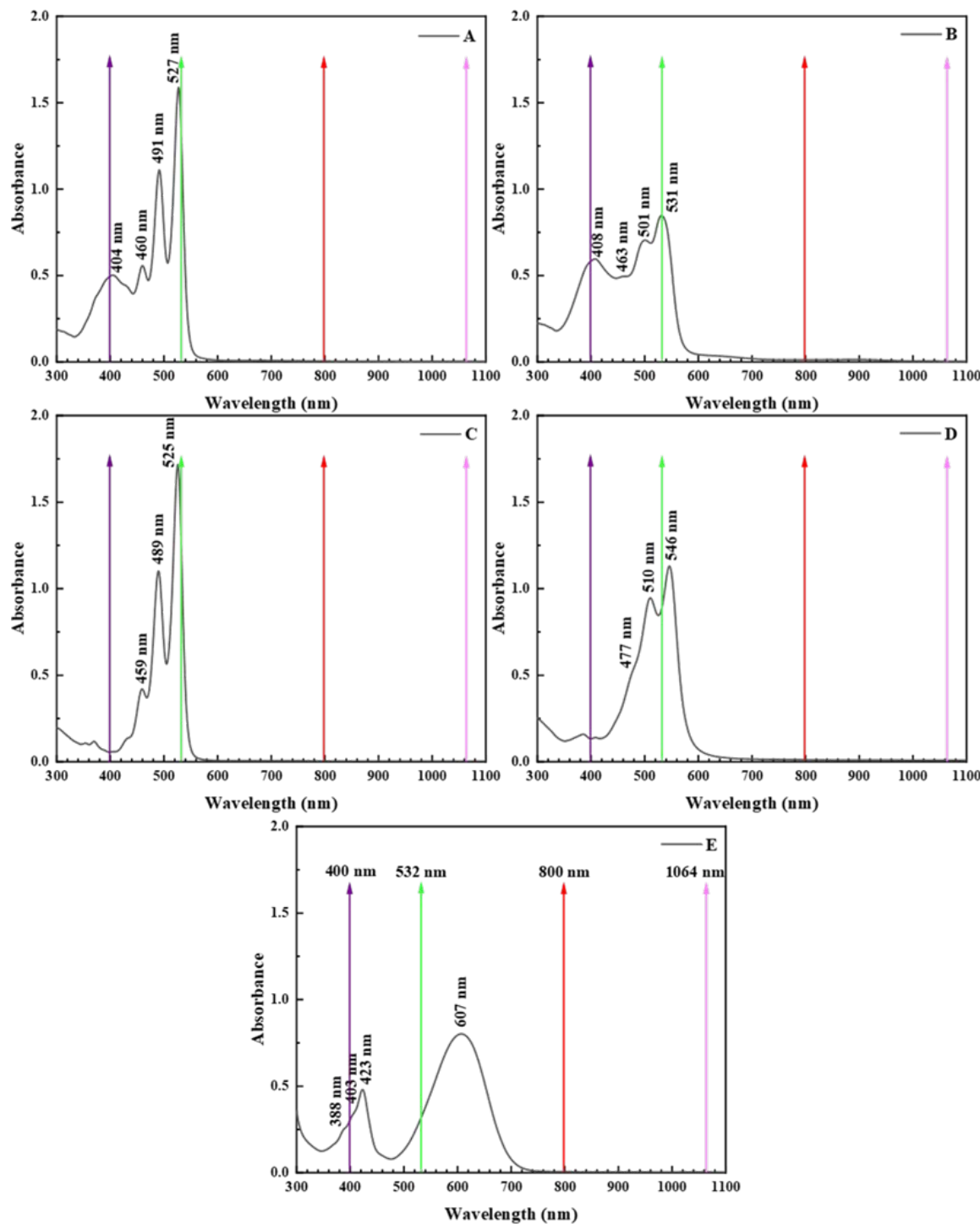


**Figure 2.** UV-Vis absorption spectra of PDI derivatives **A-E** obtained in DMF at a concentration of 0.25 mg/mL. The colored arrows indicate the wavelengths where laser excitation took place.

*Theoretical Analysis:* The UV-Vis absorption spectra of the PDI derivatives **A-E** were also calculated. The transition energies were computed by employing the time-dependent density



functional theory (TD-DFT),<sup>34</sup> using the CAM-B3LYP functional, which is known for the satisfactory estimation of the transition energies of other organic dyes, compared with the experimental results.<sup>35,36</sup> The effect of DMF as solvent was computed by the polarizable continuum model.<sup>37</sup> All the reported DFT calculations have been performed by using the Gaussian 16 software.<sup>38</sup> The obtained results are shown in **Table 1**. For comparison purposes the UV-Vis absorption spectra of perylene, *p*-NH<sub>2</sub>Azo molecules, unsubstituted PDI, and *N,N'*-di(hexylheptyl) PDI were also computed.

As can be seen in this table, there is a reasonable agreement between the theoretical and experimental excitation energies. The theoretical results reproduce satisfactorily the experimentally observed strong absorption peaks at ca. 530 nm (for **A**, **B** and **C**), the small red shift for **D** and the larger red shift for **E**, compared with **A**, **B** and **C**. Similarly, in agreement with the experimental observations, TD-DFT computations show high oscillator strength at ca. 400 nm for **A** and **B**, and smaller for **E**, **D**, and **C**. In order to describe the nature of the process, a description of the involved states and their percentage contribution is given in **Table 1**. In **Figure S10** the frontier molecular orbitals of PDI **A-E** involved in the main absorption process are also depicted. As presented, for most of the studied PDIs, the two highest occupied orbitals (HOMO-1, HOMO) and the two lowest unoccupied orbitals (LUMO, LUMO+1) take place during single excitation transition process (**Figure S10**). So, the results show that the *p*-NH<sub>2</sub>Azo group is responsible for the high absorption at ca. 400 nm, found for **A** and **B**. By considering the wavelength of the first allowed electronic transition of unsubstituted PDI and *N,N'*-di(hexylheptyl) PDI, it is ascertained that the absorptions of **A**, **B**, and **C**, determined experimentally at 532 nm, are attributed to the absorption of the PDI  $\pi$ -network. In addition, the incorporation of the two imide units in perylene, induces a red shift, ca. 86 nm, to the absorption wavelength, resulting in a more intense, HOMO->LUMO, transition.

**Table 1.** Calculated UV-Vis absorption wavelengths  $\lambda$ , oscillator strengths (*f*) and excitation descriptions of the two lowest-lying allowed electronic transitions of perylene, *p*-aminoazobenzene(*p*-NH<sub>2</sub>Azo) and PDI derivatives **A-E**. Comparison with the unsubstituted PDI and *N,N'*-di(hexylheptyl) PDI is also shown. The values were computed within DMF as solvent with CAM-B3LYP/6-311+G\* method. In parenthesis, the experimental values of  $\lambda$  are given.

Compound	$\lambda(\text{nm})/f$	Description
----------	------------------------	-------------



<b>Perylene</b>	424.5/0.755	$S_0 \rightarrow S_1$ HOMO- $\rightarrow$ LUMO (99%)
<b>Unsubstituted PDI</b>	511.7/1.234	$S_0 \rightarrow S_1$ HOMO- $\rightarrow$ LUMO(99%)
	322.79/0.325	$S_0 \rightarrow S_3$ HOMO-2- $\rightarrow$ LUMO(84%)
<i>N,N'</i> - di(hexylheptyl) <b>PDI</b>	512.9/1.288	$S_0 \rightarrow S_1$ HOMO- $\rightarrow$ LUMO(99%)
	322.60/0.272	$S_0 \rightarrow S_3$ HOMO-2- $\rightarrow$ LUMO(79%)
<i>p</i> -NH <sub>2</sub> Azo	389.7/1.195 (370) <sup>1</sup>	$S_0 \rightarrow S_1$ HOMO- $\rightarrow$ LUMO (99%)
<b>PDI derivative A</b>	513.2/1.409 (527) <sup>2</sup>	$S_0 \rightarrow S_1$ HOMO-1- $\rightarrow$ LUMO(98%)
	395.04/1.238 (404) <sup>2</sup>	$S_0 \rightarrow S_3$ HOMO- $\rightarrow$ LUMO+1(94%)
<b>PDI derivative B</b>	515.8/1.325 (531) <sup>2</sup>	$S_0 \rightarrow S_1$ HOMO-1- $\rightarrow$ LUMO (89%) HOMO- $\rightarrow$ LUMO (8%)
	400.8/1.344 (408) <sup>2</sup>	$S_0 \rightarrow S_3$ HOMO- $\rightarrow$ LUMO+1 (69,6%) HOMO- $\rightarrow$ LUMO(15,7%)
<b>PDI derivative C</b>	512.7/1.322 (525) <sup>2</sup>	$S_0 \rightarrow S_1$ HOMO-1- $\rightarrow$ LUMO(99%)
	322.3/0.265	$S_0 \rightarrow S_4$ HOMO-4- $\rightarrow$ LUMO (79%)
<b>PDI derivative D</b>	524.9/1.298 (546) <sup>2</sup>	$S_0 \rightarrow S_1$ HOMO- $\rightarrow$ LUMO( 67%) HOMO-1- $\rightarrow$ LUMO (29%)
	350.1/0.200	$S_0 \rightarrow S_3$ HOMO-2- $\rightarrow$ LUMO (79%)
<b>PDI derivative E</b>	567.9/1.003 (607) <sup>2</sup>	$S_0 \rightarrow S_1$ HOMO- $\rightarrow$ LUMO (98%)
	376.1/0.374	$S_0 \rightarrow S_2$ HOMO-1- $\rightarrow$ LUMO (85%)

<sup>1</sup> Experimental value<sup>15</sup>, <sup>2</sup> Experimental value (see **Figure 2**)

### Nonlinear optical response of PDI derivatives A-E

The NLO response of the PDIs A-E was systematically investigated under 4 ns, 532/1064 nm, and 70 fs, 800/400 nm, laser excitation conditions. For the accurate determination of the different NLO parameters (i.e., the nonlinear absorption coefficient  $\beta$  (and the related  $\text{Im}\chi^{(3)}$ ), the nonlinear refractive index parameter  $\gamma'$  (and the related  $\text{Re}\chi^{(3)}$ ) and the magnitude of the third-order nonlinear susceptibility  $\chi^{(3)}$ ) different concentration solutions of the PDIs in DMF

were prepared and studied under various laser intensities. For each PDI derivative A-E special care was taken to keep the absorbance of the system, at each excitation wavelength, low enough, to satisfy the “thin sample approximation” condition, ensuring the validity of the Z-scan technique approximations and therefore the analysis of the Z-scan data. In addition, since  $\text{Im}\chi^{(3)}$  and  $\text{Re}\chi^{(3)}$  depend on the concentration of PDI, they were normalized by the corresponding concentration,  $c$ , of each solution, providing the  $\text{Im}\chi^{(3)}/c$ , and  $\text{Re}\chi^{(3)}/c$  values, allowing for easier comparisons. Along the same lines, from the determined values of  $\chi^{(3)}$ , and the known concentration of the samples, the second hyperpolarizability  $\gamma$  of each PDI was calculated, providing the nonlinear optical response per molecule. In addition, for comparison purposes, and for calibration of the experimental setups, a  $\text{C}_{60}$ -toluene solution, and DMF and toluene, were used for the ns and fs Z-scan measurements, respectively, the details given in the ESI section. The experimental findings and the determined NLO parameters, for all the excitation conditions employed are presented in the following.

#### NLO response of PDI derivatives A-E, under 4 ns, 1064/532 nm laser excitation

First, the nonlinear absorption of the different PDIs under 4 ns, 532 nm excitation is discussed. In **Figure 3a**, some representative open aperture (OA) Z-scans of two different concentrations of PDI derivative **A** (0.03 and 0.06 mg/mL) in DMF and the neat solvent, all measured under identical experimental conditions, are illustrated. The solid symbols correspond to the experimental data points, while the continuous lines represent the fitting of the experimental data by Eq. S1. As shown, DMF exhibited negligible NLO response for the range of laser intensities employed. Therefore, the OA Z-scans of the solutions which are shown in **Figure 3a**, reveal straightforwardly the nonlinear absorption of PDI **A**, exhibiting a transmission maximum, indicating saturable absorption (SA) behavior (corresponding to negative sign nonlinear absorption coefficient  $\beta$ , i.e.,  $\beta < 0$ ). The observed SA behavior is attributed to the resonant excitation conditions occurring resulting in efficient depletion of the ground state and Pauli blocking mechanism<sup>39,40</sup> (see also the absorption spectrum of PDI derivative **A** in **Figure 2**). Similar Z-scan recordings were obtained for the other PDI derivatives, all exhibiting SA behavior (**Figure S11a**). From the fitting of the Z-scan recordings with Eq. S1, the  $\beta$  value of each concentration of PDI derivative **A** in DMF was determined, and then the corresponding values of  $\text{Im}\chi^{(3)}$  were calculated using Eq. S4. In **Figure 3b**, the dependence of the  $\beta$  values (of PDI derivative **A** in DMF shown in **Figure**



3a) on the incident laser energy is presented. As shown, they were all found not varying with the laser energy (within the experimental error), as expected for a third-order NLO process, and to scale linearly with the concentration. Similar results were obtained for PDI derivatives B-E (Figure S11c). The determined values of  $\beta$ ,  $\text{Im}\chi^{(3)}$  and  $\text{Im}\chi^{(3)}/c$  of all the different concentrations of the PDIs studied are presented in Table S1, while, for simplicity, Table 2 presents only the average values of  $\text{Im}\chi^{(3)}/c$  of the different concentration PDIs. In addition, the wavelength of the  $S_{0-1}$  transition and the ground state absorption cross-section of each PDI derivative are also listed in Table 2.

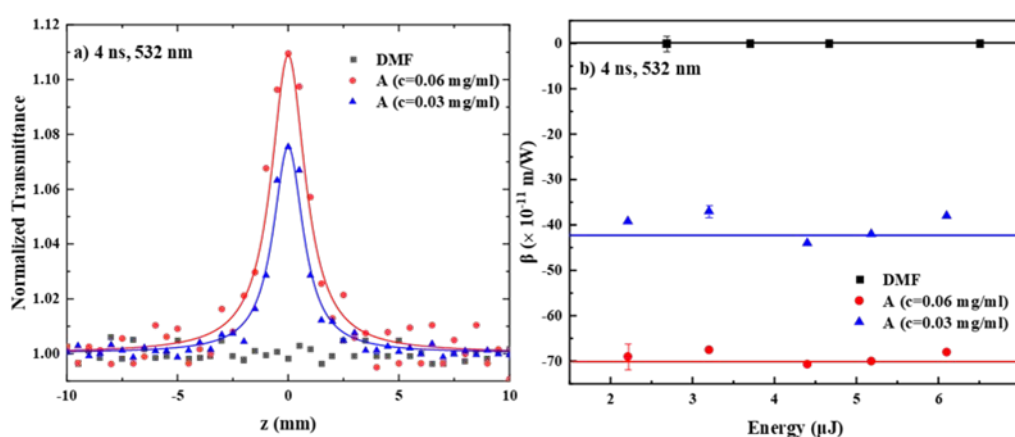


**Figure 3.** (a) OA Z-scans of two different concentrations of PDI derivative A in DMF (0.03 and 0.06 mg/mL) under 4.5  $\mu\text{J}$  (55  $\text{MW}/\text{cm}^2$ ) laser excitation, and (b) variation of the corresponding nonlinear absorption coefficient  $\beta$  with the incident laser energy, under 4 ns, 532 nm laser excitation.

Regarding the nonlinear refraction (NLR) of the PDI derivatives A-E, some representative “divided” Z-scan recordings of two different concentrations of PDI derivative A, are presented in Figure 4a. As can be seen, they exhibited a peak-valley transmittance configuration, indicative of self-defocusing behavior (corresponding to negative sign nonlinear refractive index parameter  $\gamma'$ , i.e.,  $\gamma' < 0$ ). The continuous lines correspond to the fitting of the experimental data (solid points) by Eq. S2. Since the solvent, DMF, exhibited negligible nonlinear refraction, the Z-scans of the solutions reveal directly the nonlinear refractive response of PDI derivative A. In Figure 4b, the dependence of the values of the  $\Delta T_{p-v}$  parameter (see e.g., Figure 4a) of the two solutions on the incident laser energy is shown. As can be seen, a linear dependence of the  $\Delta T_{p-v}$  on the laser energy was found in



both cases, i.e., a typical behavior for a third-order NLO process. All PDIs were found exhibiting the same sign nonlinear refractive response, i.e., self-defocusing ( $\gamma' < 0$ ) (see **Figure S11b,d**). From the slopes of the continuous straight lines of **Figure 4b**, the values of  $\gamma'$ ,  $\text{Re}\chi^{(3)}$  were determined, using Eq. S3 and Eq. S5, respectively, and then the values of  $\text{Re}\chi^{(3)}/c$  were calculated using the known concentration of the solutions. The average values of  $\text{Re}\chi^{(3)}/c$ ,  $\chi^{(3)}/c$  and  $\gamma$  of PDIs **A-E** are summarized in **Table 2**, while the values of  $\gamma'$ ,  $\text{Re}\chi^{(3)}$ ,  $\text{Re}\chi^{(3)}/c$ ,  $\chi^{(3)}/c$  and  $\gamma$  of the different concentration solutions of PDIs studied are presented in **Table S1**. To understand the NLR response of the different PDI derivatives, several mechanisms can be evoked, the contribution of each depending on the laser pulse duration and the laser intensity used. So, in general, instantaneous bound-electronic response (i.e., Kerr-type nonlinearity) or other non-instantaneous contributions, such as molecular reorientation, thermal effects and free carrier refraction, can be responsible for the observed NLR response. However, under the present 4 ns resonant excitation conditions at 532 nm (see also the absorption spectra in **Figure 2**) thermal effects should be, most probably, the dominant mechanism resulting to the observed self-defocusing NLR response.<sup>39,40</sup>

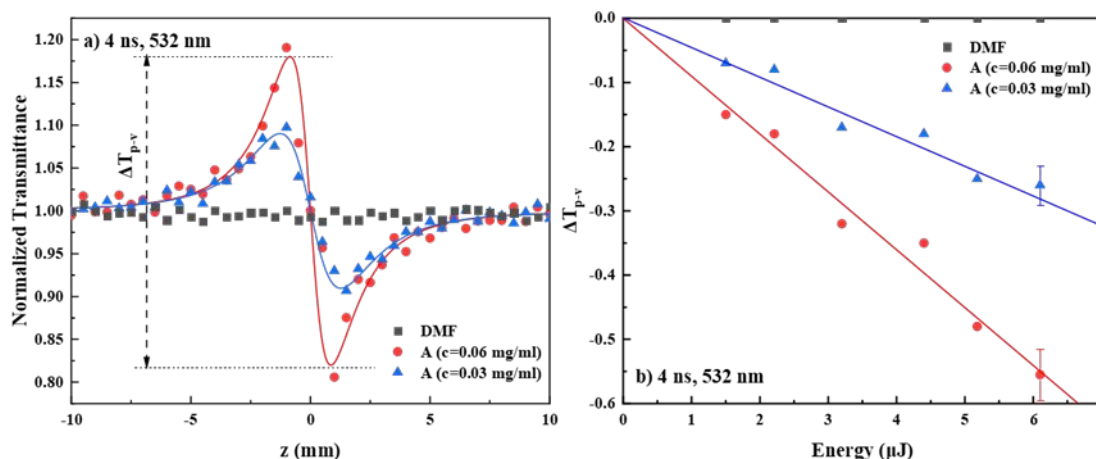


**Figure 4.** (a) “Divided” Z-scans of two different concentrations of PDI derivative **A** in DMF (0.03 and 0.06 mg/mL) under 4.5  $\mu\text{J}$  (55  $\text{MW}/\text{cm}^2$ ) laser excitation, and (b) variation of the corresponding  $\Delta T_{p-v}$  values with the incident laser energy, under 4 ns, 532 nm laser excitation.

For the investigation of the NLO response of the PDI derivatives **A-E** under 4 ns, 1064 nm laser excitation, similar Z-scan experiments were conducted using the fundamental laser output at 1064 nm. However, although much higher concentrations were used (e.g., up to  $\sim 1$



255 mg/mL) and higher laser energies were employed (e.g., up to 40  $\mu$ J), all PDIs exhibited  
256 negligible nonlinear absorption and refraction, suggesting a negligible NLO response under  
257 1064 nm excitation.

258 **Table 2.** NLO parameters of PDI derivatives **A-E** under 4 ns, 532 nm laser excitation.

Compounds	$S_{0-1}$ transition (nm)/ Ground state absorption cross-section ( $\times 10^{-19}$ cm <sup>2</sup> /mol)	$\text{Im}\chi^{(3)}/c$ ( $\times 10^{-13}$ esu mL/mg)	$\text{Re}\chi^{(3)}/c$ ( $\times 10^{-13}$ esu mL/mg)	$\chi^{(3)}/c$ ( $\times 10^{-13}$ esu mL/mg)	$\gamma$ ( $\times 10^{-34}$ esu)
PDI derivative A	527/1.56	$-705 \pm 75$	$-2040 \pm 210$	$2158 \pm 224$	$832 \pm 86$
PDI derivative B	531/1.25	$-256 \pm 26$	$-1744 \pm 122$	$1764 \pm 126$	$856 \pm 61$
PDI derivative C	525/1.30	$-509 \pm 55$	$-2115 \pm 239$	$2177 \pm 247$	$726 \pm 82$
PDI derivative D	546/1.18	$-297.7 \pm 28$	$-1557 \pm 188$	$1584 \pm 191$	$686 \pm 82$
PDI derivative E	607/0.36	$-146 \pm 14$	$-549 \pm 67$	$569 \pm 68$	$220 \pm 26$

259

260 From the inspection of the determined values of the NLO parameters of the PDIs listed in

261 **Table 2**, it is evident that they all exhibit sizeable NLO response under 4 ns, 532 nm

262 excitation. In particular, **A** and **B** exhibited the largest, and of similar magnitude (within the

263 experimental error),  $\chi^{(3)}/c$  and second hyperpolarizability  $\gamma$  values. On the other hand, **C** and

264 **D**, having also very similar NLO response, exhibited relatively lower NLO response

265 compared to **A** and **B**, while **E** exhibited the lowest NLO response among the PDI derivatives

266 studied. The evaluation of these results and the consideration of the absorption spectra of the

267 different PDI derivatives suggest that the NLO response under 4 ns, 532 nm laser excitation,

268 is largely determined by the resonant character of the excitation at this wavelength (see also

269 **Figure 2**) and from the ground state absorption cross section of each PDI as well. So, PDI

270 derivatives **A**, **B**, **C** and **D** exhibited the largest NLO response, as their excitation at 532 nm

271 is practically full resonant with the corresponding  $S_{0-1}$  electronic transition located at 527,

272 531, 525 and 546 nm, respectively (see also **Figure 2**). In contrast, in the case of PDI

273 derivative **E**, where the corresponding absorption band is red shifted at 607 nm, the resonant

274 excitation conditions are only partially met (due the large broadening of this absorption



band). Therefore, qualitatively, the closer the laser excitation occurs to the  $S_{0-1}$  transition, the stronger the NLO response of the PDI. Another parameter that should be also considered is the ground state absorption cross section  $\sigma$ , at 532 nm. In that view, from the absorbance and the concentration of each PDI derivative, the extinction coefficient  $\epsilon$ , at 532 nm, was determined, and the corresponding  $\sigma$  value was calculated. So, the ground state absorption cross sections  $\sigma$  for the various PDI derivatives were found to be as follows: **A**: 1.56, **B**: 1.25, **C**: 1.30, **D**: 1.18, and **E**: 0.36 (in units of  $10^{-20}$  cm<sup>2</sup>/mol). It is worth noting that PDI derivative **E** exhibits the lowest absorption cross-section.

Another interesting finding, resulting from the above results, concerns the influence of the type of anchored group on the PDI core. So, the anchoring of *p*-aminoazobenzene group (i.e., PDIs **A** and **B**) was found to result in larger NLO response than that of aniline (i.e., PDIs **C** and **D**), or amino groups (i.e., PDI **E**). Interestingly, the place of substitution (i.e., at the imide- or bay-position) seems to have a weaker effect on the NLO response.

#### NLO response of PDI derivatives A-E, under 70 fs, 800/400 nm laser excitation

Next, the results concerning the NLO response of the PDI derivatives **A-E** under 70 fs laser excitation are presented. In this case, the excitation was performed at 800 and 400 nm, in order to study the influence of the non-resonant and resonant excitation conditions, respectively, on the NLO response of the various PDIs.

At first, some representative OA Z-scans of two different concentrations of PDI derivative **B** in DMF (0.25 and 0.50 mg/mL) and the neat solvent are presented in **Figure 5a**. As shown, DMF exhibited negligible nonlinear absorption. So, the OA Z-scans of the solutions reveal straightforwardly the nonlinear absorption behavior of **B**, i.e., a transmission minimum, indicating reverse saturable absorption (RSA) behavior (corresponding to positive sign nonlinear absorption coefficient  $\beta$ ,  $\beta > 0$ ). From the absorption spectrum of **B** (see e.g., **Figure 2**), it can be easily seen that excitation at 800 nm is not resonant with any absorption band; however, when considering the high intensity of the fs laser excitation, TPA becomes very probable and readily occur; this TPA process is further assisted by the presence of the 400 nm absorption band, which can be attained by the absorption of two photons. Based on these experimental findings, the observed RSA behavior can be attributed to TPA, as has been discussed in detail elsewhere.<sup>39</sup> In **Figure 5b**, the variation of the  $\beta$  values of the two



concentration solutions of PDI derivative **B** of **Figure 5a**, with the laser energy is depicted. As shown, they were found to be independent on the incident laser energy and scaling linearly with the concentration of **B**. Similar experiments were performed using different concentrations of **A**, **C**, **D** and **E**, all in DMF, revealing that all PDI derivatives exhibit RSA behaviour as well (**Figure S12a,c**). From the OA Z-scans, the nonlinear absorption coefficient  $\beta$  of each sample was determined following the same procedure as for the analysis followed for the ns measurements. Then, from the determined values of  $\beta$ , the corresponding TPA cross-section of each PDI was calculated, using Eq. S8. The obtained values of  $\text{Im}\chi^{(3)}/c$  and the TPA cross-section at 800 nm of all PDIs **A-E** are summarized in **Table 3**; the values of  $\beta$ ,  $\text{Im}\chi^{(3)}$ ,  $\text{Im}\chi^{(3)}/c$  of all the different concentration solutions studied are presented in **Table S2**.

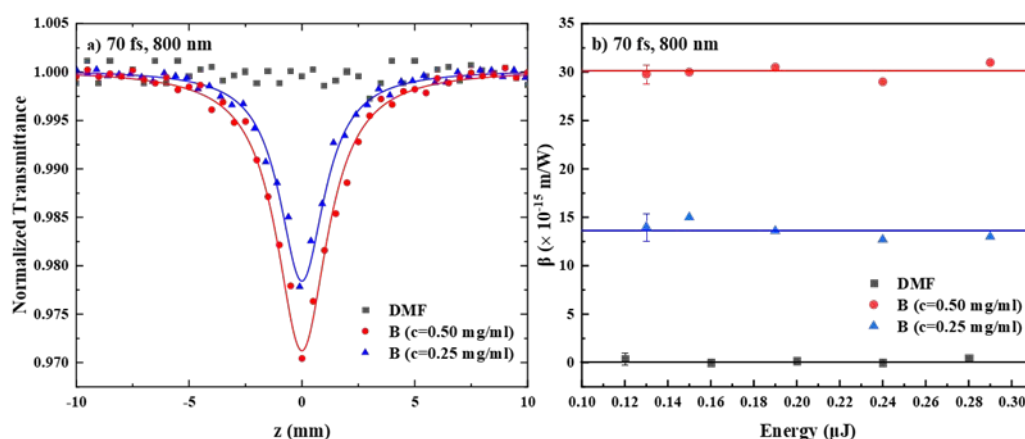


**Figure 5.** (a) OA Z-scans of two different concentrations of PDI derivative **B** in DMF (0.25 and 0.50 mg/mL) under 0.23  $\mu\text{J}$  (335  $\text{GW}/\text{cm}^2$ ) laser excitation, and (b) variation of the corresponding nonlinear absorption coefficient  $\beta$  with the incident laser energy, under 70 fs, 800 nm laser excitation.

Next, the results concerning the nonlinear refraction of PDI derivatives **A-E** under 70 fs, 800 nm excitation are presented and discussed. So, in **Figure 6a**, the “divided” Z-scans of the two different concentrations of **B** shown in **Figure 5a** are presented, as an example; they were both found exhibiting a valley-peak transmittance configuration, indicative of self-focusing behavior (corresponding to positive nonlinear refractive parameter  $\gamma'$ ,  $\gamma' > 0$ ). However, similar measurements of neat DMF, performed under identical experimental conditions, have shown that it exhibited significant nonlinear refraction (see e.g., black line in **Figure 6a**) of positive sign (i.e., self-focusing), as well. Therefore, for the determination





of the nonlinear refractive index parameter  $\gamma'$  of the PDIs, DMF's contribution was considered accordingly. More experiments performed on different concentrations of PDIs **A**, **C**, **D** and **E** have shown that the corresponding “divided” Z-scans were indistinguishable from those of neat DMF (see also **Figure S12b,d**). This situation was further confirmed employing up to ten times higher concentrations of **A**, **C**, **D** and **E** (i.e., up to 2.5 mg/mL) in DMF. So finally, only the nonlinear refraction of **B** was possible to be determined accurately.

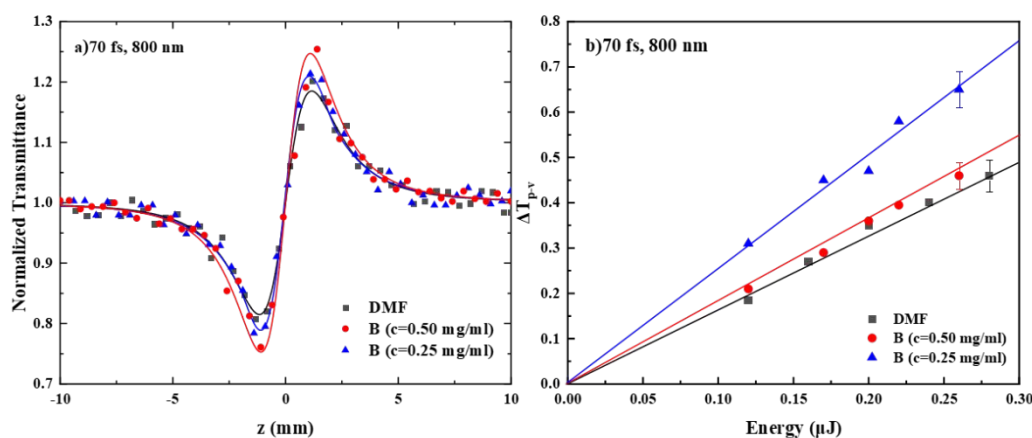


**Figure 6.** (a) “Divided” Z-scans of two different concentrations of PDI derivative **B** in DMF (0.25 and 0.50 mg/mL) under 0.23  $\mu$ J (335 GW/cm<sup>2</sup>) laser excitation, and (b) variation of the  $\Delta T_{p-v}$  values, under 70 fs, 800 nm fs laser excitation.

In **Figure 7a**, some representative OA Z-scans of two different concentrations of PDI derivative **B** (0.04 and 0.08 mg/mL) in DMF and the neat solvent, obtained under 400 nm excitation, are presented. In this case, DMF had significant NLO response, exhibiting a transmission minimum, indicative of RSA behavior (i.e.,  $\beta > 0$ ), while all PDIs' solutions were found to exhibit a smaller transmission minimum, revealing opposite sign nonlinear absorption, i.e., SA. In fact, all PDIs exhibited similar behavior, i.e., negative nonlinear absorption coefficient,  $\beta < 0$  (see e.g., **Figure S13a,b**). For the accurate determination of the nonlinear absorption coefficient  $\beta$  of **A-E**, the contribution of DMF was considered accordingly. The variation of the determined  $\beta$  values of the two concentrations of **B** of **Figure 7a** with the incident laser energy is presented in **Figure 7b**. As can be seen, the  $\beta$  values of the two solutions were found independent on the incident laser energy and scaling linearly with the concentration. The average values of  $\text{Im}\chi^{(3)}/c$  of the different concentration



of **A-E** are summarized in **Table 3**, while the values of  $\beta$ ,  $\text{Im}\chi^{(3)}$  and  $\text{Im}\chi^{(3)}/c$  of the different concentrations of the PDIs studied are presented in **Table S2**.

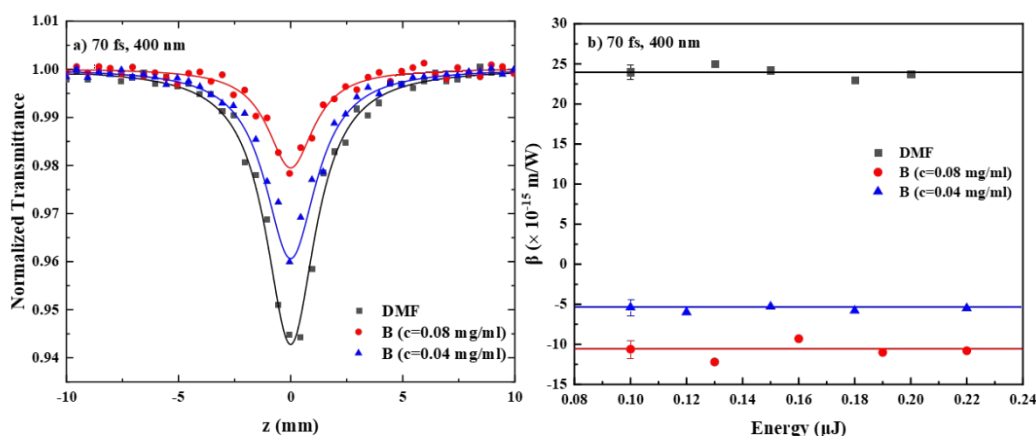


**Figure 7.** (a) OA Z-scans of two different concentrations of PDI derivative **B** in DMF (0.04 and 0.08 mg/mL) under 0.12  $\mu\text{J}$  (382  $\text{GW}/\text{cm}^2$ ) laser excitation, and (b) variation of the corresponding nonlinear absorption coefficient  $\beta$  with the incident laser energy, under 70 fs, 400 nm laser excitation.

Concerning the nonlinear refraction of PDI derivatives **A-E** under 400 nm laser excitation, the corresponding “divided” Z-scans were found to exhibit a valley-peak transmittance configuration, indicative of self-focusing behavior (corresponding to positive nonlinear refractive parameter  $\gamma'$ ,  $\gamma' > 0$ ). As an example, the “divided” Z-scans of the two different concentrations of **B** (of **Figure 7a**) in DMF are shown in **Figure 8a**. Separate measurements of neat DMF, under identical experimental conditions, have shown that it also exhibits positive sign nonlinear refraction (i.e., self-focusing). Therefore, for the determination of the nonlinear refractive index parameter  $\gamma'$ , the solvent’s contribution was considered accordingly. In **Figure 8b**, the variation of the  $\Delta T_{p-v}$  values of the two different concentrations of **B** in DMF, and neat DMF, as a function of the incident laser energy, is shown. As can be seen,  $\Delta T_{p-v}$  was found varying linearly with the incident laser energy, in agreement with a third-order nonlinear optical process. Similar behavior was found for PDIs **A**, **C**, **D** and **E** (see **Figure S14c,d**). Then, the values of  $\gamma'$  and  $\text{Re}\chi^{(3)}$  were determined using Eq. S3 and Eq. S5, respectively, and the corresponding values of  $\text{Re}\chi^{(3)}/c$  were calculated using the known concentration of each solution. In **Table 3**, the average values of  $\text{Re}\chi^{(3)}/c$



and  $\chi^{(3)}/c$  of each PDI, are presented; the  $\gamma'$ ,  $\text{Re}\chi^{(3)}$ ,  $\text{Re}\chi^{(3)}/c$ ,  $\chi^{(3)}/c$  and  $\gamma$  values of the different concentrations studied are summarized in **Table S2**. Regarding the origin of the NLO refraction of the PDI derivatives under fs excitation, this can be attributed to the instantaneous bound-electronic response of the molecules, (i.e., Kerr-type nonlinearity).<sup>41</sup>

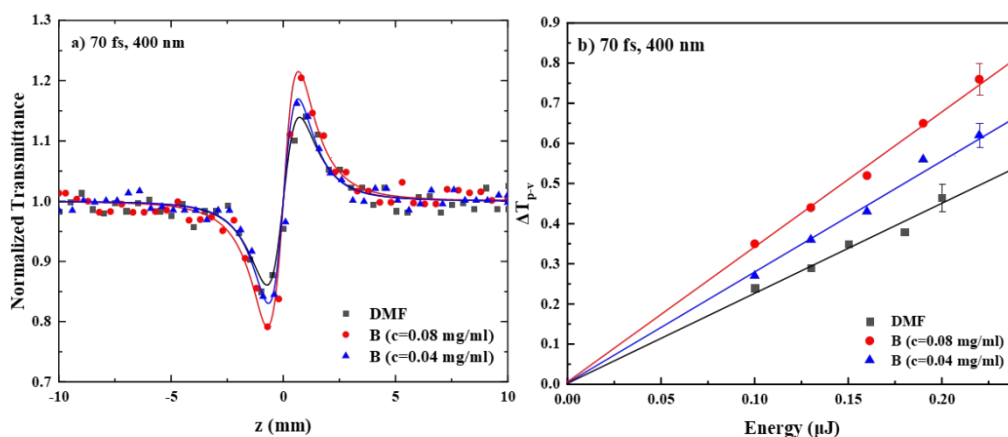


**Figure 8.** (a) “Divided” Z-scans of two different concentrations of PDI derivative **B** in DMF (0.04 and 0.08 mg/mL) under 0.12  $\mu\text{J}$  (382  $\text{GW}/\text{cm}^2$ ) laser excitation, and (b) variation of the  $\Delta T_{p-v}$  values, under 70 fs, 400 nm fs laser excitation.

**Table 3.** NLO parameters of PDI derivatives **A-E** under fs excitation at 800 and 400 nm.

$\lambda_{\text{exc}}$ (nm)	Compounds	TPA cross-section ( $\times 10^{-47} \text{ m}^4 \text{ s/photon}$ molecule)	$\text{Im}\chi^{(3)}/c$ ( $\times 10^{-16} \text{ esu}$ mL/mg)	$\text{Re}\chi^{(3)}/c$ ( $\times 10^{-16} \text{ esu}$ mL/mg)	$\chi^{(3)}/c$ ( $\times 10^{-16} \text{ esu}$ mL/mg)	$\gamma$ ( $\times 10^{-37}$ esu)
800	PDI derivative A	$13.0 \pm 1.0$	$21.6 \pm 1.2$	-	$21.7 \pm 1.2$	$8.4 \pm 0.3$
	PDI derivative B	$22.0 \pm 2.0$	$29.4 \pm 2.7$	$1.5 \pm 0.3$	$30.0 \pm 2.1$	$14.4 \pm 1.1$
	PDI derivative C	$5.8 \pm 0.5$	$9.4 \pm 1.2$	-	$10.8 \pm 1.6$	$3.6 \pm 0.5$
	PDI derivative D	$11.0 \pm 2.0$	$15.8 \pm 1.8$	-	$15.8 \pm 1.8$	$6.8 \pm 1.0$
	PDI derivative E	$12.0 \pm 0.6$	$18.6 \pm 0.6$	-	$18.6 \pm 2.1$	$7.3 \pm 0.8$

$\lambda_{\text{exc}}$ (nm)	Compounds	Ground state absorption cross- section ( $\times 10^{-19} \text{ cm}^2/\text{mol}$ )	$\text{Im}\chi^{(3)}/c$ ( $\times 10^{-16} \text{ esu}$ mL/mg)	$\text{Re}\chi^{(3)}/c$ ( $\times 10^{-16} \text{ esu}$ mL/mg)	$\chi^{(3)}/c$ ( $\times 10^{-16} \text{ esu}$ mL/mg)	$\gamma$ ( $\times 10^{-37}$ esu)
400	PDI derivative A	0.52	$-16.8 \pm 0.8$	$87.5 \pm 4.6$	$88.7 \pm 4.2$	$34.2 \pm 1.6$
	PDI derivative B	0.94	$-32.5 \pm 4.2$	$109.4 \pm 8.8$	$119.0 \pm 10.1$	$57.8 \pm 5.1$
	PDI derivative C	0.04	$-2.2 \pm 0.1$	$5.0 \pm 0.8$	$6.2 \pm 0.8$	$2.0 \pm 0.2$



	<b>PDI derivative D</b>	0.17	-3.4 ± 1.1	14.1 ± 0.8	14.4 ± 1.4	6.1 ± 0.6
	<b>PDI derivative E</b>	0.26	-21.1 ± 1.0	21.2 ± 4.9	29.9 ± 3.5	11.6 ± 1.3

**C. Theoretical study of second hyperpolarizability of PDI derivatives A-E**

In order to investigate the effect of the structural alterations of the PDI derivatives **A-E** on their NLO response (structure-property relationship), the static and frequency-dependent electronic second hyperpolarizabilities,  $\gamma(0;0,0,0), \gamma(-\omega; \omega, -\omega, \omega)$  (hereinafter referred to as  $\gamma(0)$  and  $\gamma(\omega)$ , respectively), were computed.

**Computational methods**

The energy  $E(F)$  of a molecule, placed in a uniform electric field, is given by the following equation:

$$E(F) = E^0 - \mu_i F_i - \alpha_{ij} F_i F_j - \beta_{ij} F_i F_j F_k - \gamma_{ijkl} F_i F_j F_k F_l \tag{1}$$

where  $E^0$  is the field free energy;  $\mu_i$ ,  $\alpha_{ij}$ ,  $\beta_{ijk}$  and  $\gamma_{ijkl}$  are the dipole moment, the polarizability, the first hyperpolarizability and the second hyperpolarizability components, respectively. A summation over repeated indices is implied.

For the computation of the second hyperpolarizability ( $\gamma$ ) the following equation was used:

$$\gamma = \frac{1}{5} (\gamma_{xxxx} + \gamma_{yyyy} + 2\gamma_{xxyy} + 2\gamma_{xxzz} + 2\gamma_{yyzz}) \tag{2}$$

All the static electronic hyperpolarizability components,  $\gamma_{ijkl}$ , have been computed by employing finite field techniques,<sup>42</sup> using Eq. (1), by applying a step field ( $F$ ) of 0.0008 a.u. To ensure the numerical stability, the Romberg method has been used to calculate the (hyper)polarizabilities ( $\gamma_{iiii}$ ),<sup>43,44</sup> by employing field strengths of magnitude  $2^m F$ , where  $m=0-4$  and a base field of 0.0002 a.u. For all computations the energy was converged to  $10^{-11}$  a.u. The reported hyperpolarizability data have been computed by employing the CAM-B3LYP functional,<sup>45</sup> where the latter accounts for the long-range corrections, in connection with the 6-311G and 6-311+G\* basis sets. It is reminded that these methods have provided satisfactory hyperpolarizability values for several related compounds.<sup>46</sup> All PDI derivatives **A-E** have been optimized by using the M062-X functional,<sup>47</sup> in connection with the 6-311G basis set. This functional has been shown to predict satisfactorily the geometries of  $\pi$ -conjugated systems, due to the appropriate amount (54%) of the included HF exchange.<sup>48</sup> Vibrational analysis was employed to confirm that the computed structures



correspond to a minimum on the potential energy surface. To all reported hyperpolarizability computations the structures have been rotated so that their dipole moment coincides with z-axis. The effect of DMF as solvent on the static electronic (hyper)polarizabilities was computed by the polarizable continuum model.<sup>35</sup> All the reported DFT second hyperpolarizability calculations have been performed by using the Gaussian 16 software.<sup>38</sup> For the case of PDI derivatives **A-E**, the frequency-dependent second hyperpolarizability ( $\gamma(-\omega; \omega, -\omega, \omega)$ ) for  $\omega=0.0569$  a.u. ( $\lambda=800$ nm), has also been calculated with the aid of cubic response functions, as are implemented in the DALTON software.<sup>49</sup> As shown in **Table 4**, although the static hyperpolarizabilities correspond to an excitation frequency,  $\omega \rightarrow 0$ , their computation is very useful for a relative and meaningful comparison of  $\gamma$  changes between the different PDIs, since they are good approximations to the values of the dynamic hyperpolarizabilities, in the case of off-resonant excitation. In that context, the present calculations are used to address and shed light on the different issues for the better understanding of the experimental second hyperpolarizability data obtained for PDI derivatives **A-E**.

**Table 4.** Average static ( $\gamma(0)$ ) and frequency-dependent ( $\gamma(\omega)$ ) second hyperpolarizability values of PDI derivatives **A-E**, computed with CAM-B3LYP/6-311G method, within DMF as solvent. All values are given in esu.

Compounds	$\gamma(0) (\times 10^{-34})$	$\gamma(\omega) (\times 10^{-34})^1$
PDI derivative A	13.3	55.9
PDI derivative B	15.3	64.5
PDI derivative C	8.7	30.9
PDI derivative D	9.5	40.0
PDI derivative E	8.8	42.8

<sup>1</sup>  $\gamma(-\omega; \omega, -\omega, \omega)$ ,  $\omega=0.05695$  a.u. ( $\lambda=800$  nm)

### Theoretical analysis

In **Figure 9** the results of  $\gamma(0)$  for PDI derivatives **A-E**, computed with CAM-B3LYP/6-311+G\* method, are depicted. For comparison, the  $\gamma(0)$  values of perylene, unsubstituted PDI, and *N,N'*-di(hexylheptyl) PDI are also shown.



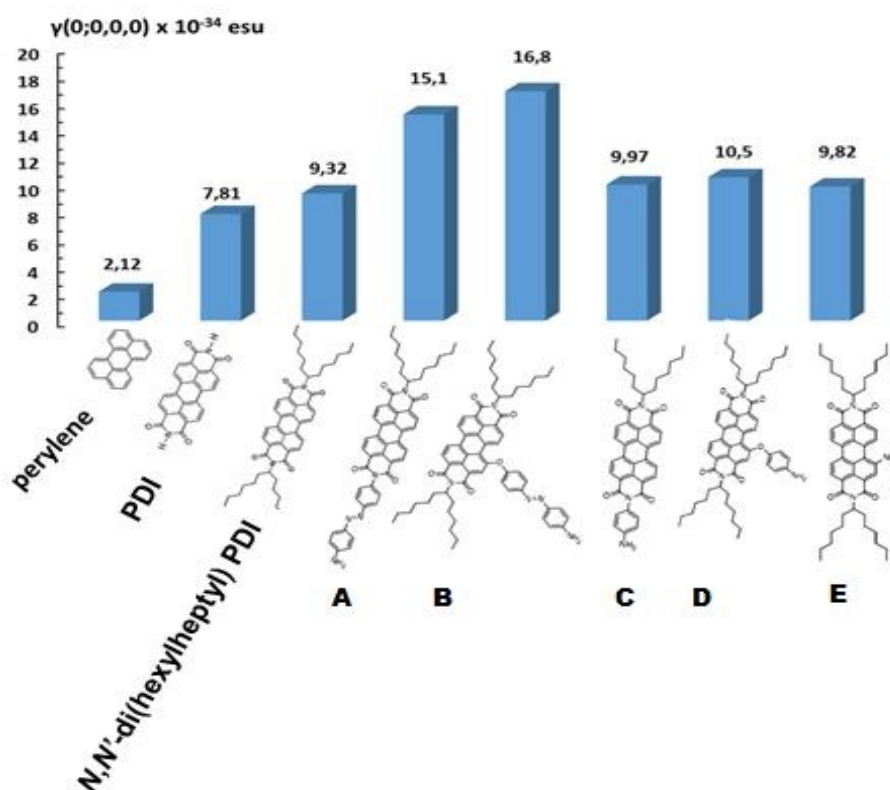


**Figure 9.** Average static electronic second hyperpolarizabilities of perylene, unsubstituted PDI, *N,N'*-di(hexylheptyl) PDI, and PDI derivatives A-E (from left to right). Values were computed with CAM-B3LYP/6-311+G\* method within DMF as solvent. All geometries were optimized with M062-X/6-311G method.

### Electronic second hyperpolarizability $\gamma$

In order to study and understand how the derivatization of PDI modifies its polarization character and NLO response, the alteration of the second hyperpolarizability between the PDI derivatives A-E is analyzed in terms of: a) the group type, and b) the anchoring position.

*Group Type:* Three types of functionalization groups were considered: *para*-aminoazobenzene (*p*-NH<sub>2</sub>Azo), aniline (AN) and amine (NH<sub>2</sub>). It is observed that when the group is anchored on the bay position of the PDI, e. g. derivatives B, D and E, the following trend was found:  $\gamma(0)[B] >> \gamma(0)[D] \geq \gamma(0)[E]$ . For an evaluation of the effect of the functionalization groups on the second order hyperpolarizability of the PDIs, the ratio  $k(X) = \gamma(X)/\gamma(Y)$  is used, where X=B, D, E, and Y=unsubstituted PDI. It was found that for B, D and E, this ratio is  $k(B)=2.01$ ,  $k(D)=1.26$ ,  $k(E)=1.17$ , respectively.





A similar trend of the  $\gamma$  values is observed when the group is anchored at the imide position, as e.g. for derivatives **A** and **C**, where  $\gamma(0)[\mathbf{A}] > \gamma(0)[\mathbf{C}]$ , while the ratio  $k(\mathbf{X})$ :  $k(\mathbf{X}) = \gamma(\mathbf{X})/\gamma(\mathbf{Y})$ , where  $\mathbf{X} = \mathbf{A}$ , **C**, and  $\mathbf{Y} =$  unsubstituted PDI, was found to be:  $k(\mathbf{A}) = 1.81$ ,  $k(\mathbf{C}) = 1.19$ . From the previous analysis it is evident that the largest change on the second hyperpolarizability is observed for the *p*-NH<sub>2</sub>Azo group, implying its high polarization character and high contribution to the second hyperpolarizability.

*Anchoring Position:* Two positions of group anchoring were examined: the bay and imide positions. It is noted that  $\gamma(0)[\mathbf{B}] > \gamma(0)[\mathbf{A}]$  and  $\gamma(0)[\mathbf{D}] > \gamma(0)[\mathbf{C}]$ . Similar trends were also observed for the frequency-dependent computed values, whereas  $\gamma(\omega)[\mathbf{B}] > \gamma(\omega)[\mathbf{A}]$ , and  $\gamma(\omega)[\mathbf{C}] > \gamma(\omega)[\mathbf{D}]$ ,  $\omega = 0.05695$  a.u. (**Table 4**). By considering the above defined ratios,  $k(\mathbf{X})$ , it is also observed that  $k(\mathbf{B})/k(\mathbf{A}) = 1.1$  and  $k(\mathbf{D})/k(\mathbf{C}) = 1.06$ . These findings imply that group (*p*-NH<sub>2</sub>Azo, AN) anchoring at the bay position of the PDI (i.e., derivatives **B**, **D**, and **E**) induces higher changes on  $\gamma(0)$  resulting in larger values, compared with those computed when the group is connected at the imide position. From the previous analysis it is ascertained that the higher alteration on the second hyperpolarizability is achieved by bay anchoring in connection with the *p*-NH<sub>2</sub>Azo group.

It is interesting to note that, as observed, the incorporation of the two imide units on the perylene skeleton has a large effect on the second hyperpolarizability value. Therefore, it is seen that  $\gamma(0)[\mathbf{Y}] = 4.34 \times \gamma(0)[\mathbf{P}]$ , where  $\mathbf{Y}$  is the unsubstituted PDI (see **Figure 9**). Further *N,N'*-di(hexylheptyl) substitution of PDI has a weaker effect, as the second hyperpolarizability exhibits a smaller enhancement by a factor of 1.3.

### Theoretical interpretation of the second hyperpolarizability

In order to get a better insight into the origin of the alteration of  $\gamma(0)$  values and the observed trends between the PDIs **A-E**, the second hyperpolarizability density was evaluated as well. Hyperpolarizability density is associated with the spatial distribution and characteristics of a molecule's or material's response to a strong electric field. It provides a qualitative way to visualize the electron density fluctuations, responsible for the observed NLO phenomena, thus revealing the regions of the molecule contributing most to the NLO response. Since hyperpolarizability density analysis can map the electron density of a molecule which is most susceptible to polarization, it provides a particularly useful way in understanding how molecular and electronic structures influence the NLO properties.



Since the aromatic core of the PDI lies e.g. on a ZY plane, only the in-plane diagonal components,  $\gamma_{zzzz}$  and  $\gamma_{yyyy}$ , of the PDIs are studied, as they are expected to have a larger contribution to  $\gamma$  (see **Table S3**). For the needs of the analysis, the functions  $-z\rho_{zzz}^{(3)}(r)$  and  $-y\rho_{yyy}^{(3)}(r)$ , were computed, where the function  $\rho_{zzz/yyy}^{(3)}(r)$  is associated with the third-order derivative of the electron density with respect to the field:

$$\rho_{zzz/yyy}^{(3)}(r) = \left. \frac{\partial^3 \rho_i(r)}{\partial F_{z/y}^3} \right|_{F=0}$$

These functions provide a way to map the regions of the molecule that contribute in a positive or negative way to its overall second hyperpolarizability  $\gamma$ . Additionally, their integration (i.e.,  $\gamma_{zzzz} = -\int z\rho_{zzz}^{(3)}(r)dr$ ,  $\gamma_{yyyy} = -\int y\rho_{yyy}^{(3)}(r)dr$ ) allows for the determination of the  $\gamma_{zzzz}/\gamma_{yyyy}$  ratio and its comparison with the value obtained by numerical differentiation.

The  $-z/y\rho_{zzz/yyy}^{(3)}(r)$  plots are depicted in **Figure S15**. In order to decrease the computational cost, the functions  $\rho_{zzz/yyy}^{(3)}(r)$  were computed with CAM-B3LYP/6-311G method. As shown in **Table 4**, these  $\gamma(0)$  values are a good approximation to the corresponding dynamic ones, computed far from resonance at  $\lambda=800$  nm. Additionally, as provided in **Table S4**, the  $\gamma(0)$  values computed with the smaller basis set (6-311G), adequately convey the changes and the trends of the second hyperpolarizability between the different PDI derivatives **A-E**, when compared with the corresponding PDI  $\gamma$  values computed with the larger (6-311+G\*) basis set. The calculation of the  $\rho_{zzz/yyy}^{(3)}(r)$  functions was performed with the Multiwfn software.<sup>50</sup>

In general, the computed density plots of  $\gamma$  (see also **Figure S15**) were found to fully support and corroborate the previous findings. So, for all PDI derivatives **A-E**, the positive contribution was found to be larger and mostly distributed along the  $\pi$  network and at a lesser extent to the bay of the PDI core (upon group introduction), thus explaining the computed large and positive  $\gamma_{zzzz}$  and  $\gamma_{yyyy}$  values of the **A-E** derivatives.

Bay substitution (e.g. PDI derivatives **B**, **D**, and **E**) imposes large changes on the  $\gamma_{zzzz}$  density and even larger on the  $\gamma_{yyyy}$  one, expanding the molecular areas that contribute positively to the  $\gamma$ . The largest influence on  $\gamma_{zzzz/yyy}$  densities is observed upon introduction of the trans isomer of *p*-NH<sub>2</sub>Azo group; this can explain the largest second hyperpolarizability found both experimentally and theoretically (i.e., upon excitation at 400 nm) for **B**. It is interesting





to note that for this PDI derivative, a large negative contribution to  $\gamma_{zzzz/yyyy}$  density is localized within the region connecting the  $\pi$ -network of PDI and the  $p$ -NH<sub>2</sub>Azo molecular unit. It is also highlighted that the presence of the  $p$ -NH<sub>2</sub>Azo, in its trans configuration, considerably expands the areas of the molecule which contribute positively to  $\gamma$ , compared with those found for **D** and **E**. This finding explains the origin of the larger second hyperpolarizability value computed for **B**, compared with those found for **D** and **E**. Moreover, it strengthens our conclusion concerning the influence of the  $p$ -NH<sub>2</sub>Azo group to the polarization properties of the PDIs and the observed changes imposed to  $\gamma$ .

On the other hand, substitution at the imide position with  $p$ -NH<sub>2</sub>Azo or aniline (e.g., PDIs **A** and **C**), drastically affects the density of the  $\gamma_{zzzz}$  component, by expanding significantly the area of the molecule with positive contribution. It is seen that introduction of the trans  $p$ -NH<sub>2</sub>Azo group, at the imide position of the PDI core, expands largely the area with positive contribution to  $\gamma_{zzzz}$ . Similarly to what observed for derivative **B**, the largest negative contribution to  $\gamma_{zzzz}$  density is localized on the area connecting the  $\pi$ -network of the PDI with the  $p$ -NH<sub>2</sub>Azo molecular unit, whereas a large positive contribution is localized at the terminal aniline group of the  $p$ -NH<sub>2</sub>Azo. Introduction of the aniline group (e.g., PDI **C**), increases, in a similar way, the positive contribution to the  $\gamma_{zzzz}$  density, although at a lower degree compared with derivative **A**, thus justifying the larger second hyperpolarizability found for **A**. Overall it is observed that PDI group anchoring can significantly alter the molecular regions which contribute positively/negatively to the second hyperpolarizability density, thus tuning their overall NLO response.

**Structural conformation upon group anchoring.** The optimized geometries of the different PDI derivatives are depicted in **Figure S16**. It is seen that for **A** and **C**, where the group is anchored at the imide position, the PDI core is planar. However, for **B**, **D** and **E**, where the group anchoring occurs at the bay position, the PDI core is twisted at its center, due to steric effects, similar to what was previously reported elsewhere.<sup>51,52</sup> All the anchored groups ( $p$ -NH<sub>2</sub>Azo, aniline and NH<sub>2</sub>), attached either to the bay or imide position, are twisted with respect to the  $\pi$ -conjugated PDI core. The degree of rotation depends on both the type of the anchored group and the anchoring position as well. In the case of **A** and **C**, the degree of twisting is similar, ca 61°-62°, while for **D**, aniline's twisting-with respect to the  $\pi$ -conjugated core-is larger compared with the corresponding of  $p$ -aminoazobenzene in **B**. It is noteworthy



that, as expected (*vide supra*), the ether linkage in **B** leads to a non-orthogonal arrangement of the PDI core and the azobenzene subunit (dihedral angle 47.5°, **Figure S16**). This allows the HOMO of **B** to spread over the complete  $\pi$ -system, while the LUMO, although mainly located on the PDI, shows some contribution of the azobenzene moiety (**Figure S10**).

The observed structural distortions, upon functionalization, influence the distribution of the second hyperpolarizability density (see e.g. **Figure S15**). It is observed that in the case of **A** and **B**, where the anchored functional group is the highly polarized *p*-NH<sub>2</sub>Azo, distortion results in the formation of two non-overlapping density areas, contributing either positively or negatively to the second hyperpolarizability. The high negative contribution is localized on the phenylene group of *p*-NH<sub>2</sub>Azo, anchored either to the imide side, as in **A**, or to the bay side, as in **B**, whereas the positive contribution is localized on the terminal aniline group of *p*-NH<sub>2</sub>Azo. A similar picture, although to a lesser degree concerning the extent of the  $\gamma$  positive/negative density areas, is observed for **C** and **D**, where aniline is the anchored group.

### Comparison of the experimental with the theoretical results

As it is known<sup>53</sup> the non-linear optical response of a material can be related to various physical mechanisms that occur at different time scales and contribute to the overall macroscopic NLO response. The relative contribution of each mechanism on the induced NLO response, depends on different parameters, that can be related to the laser source (e.g. laser intensity, wavelength, CW or pulsed operation, low or high repetition rate, laser pulse duration, etc.), the material itself (e.g., chemical composition, crystal structure, dielectric or metallic character, etc.) and the environment of the atoms/molecules (e.g., solution, thin film, etc.). In the case of fs laser excitation, the NLO response is mainly due to the distortion of the electronic cloud and is usually referred as instantaneous electronic response and occurs in the time scale of 10<sup>-15</sup> s. When longer duration laser pulses are used for excitation, as e.g., ps or ns, several other mechanisms can take place, as e.g., molecular vibrations, intermolecular interactions, thermal diffusion processes, population redistribution within the excited states etc, the relative contribution of each mechanism on the macroscopic NLO response being mainly determined by the laser pulse duration and the laser repetition rate. So, under ns excitation, although all or some of these physical mechanisms can contribute to the NLO response, population redistribution among the excited states is usually the dominant mechanism, and is usually referred as effective NLO response, and the corresponding NLO



parameters as effective ones. Based on the above, the results obtained from the theoretical calculations are comparable with the instantaneous electronic response of the studied PDIs, i.e., to the experimental results obtained under 70 fs, 800 nm laser excitation conditions, i.e., under fs non-resonant excitation.

In **Figure 10**, the comparison of the experimentally determined and the computed values of the second hyperpolarizability  $\gamma$ , is schematically presented. As can be observed the DFT results, concerning the alterations of the second hyperpolarizability upon side anchoring (bay, imide) and type of group, are qualitatively in excellent agreement with the experimental results, both following the same trend. For PDI derivatives **A** and **B**, where the *p*-aminoazobenzene group is anchored, the calculations predict larger  $\gamma$  values, compared to those found for **C**, **D** and **E**, in excellent agreement with the reported experimental data. Similarly, the experimentally determined larger NLO response of the bay substituted PDIs **B** and **D**, compared to that of the imide substituted ones **A** and **C**, is also confirmed by the computations. These findings validate that the computed DFT NLO values can predict successfully the effect of the structure-property relationship on the second hyperpolarizability of the PDI derivatives, as provided by the analysis of the second hyperpolarizability density. Let us also note that the observed discrepancy of the absolute magnitudes between experimental and theoretical  $\gamma$  values originates from the fact that second hyperpolarizability measurement is made by applying an oscillating optical field, instead of a static field used for the computations<sup>54,55</sup>



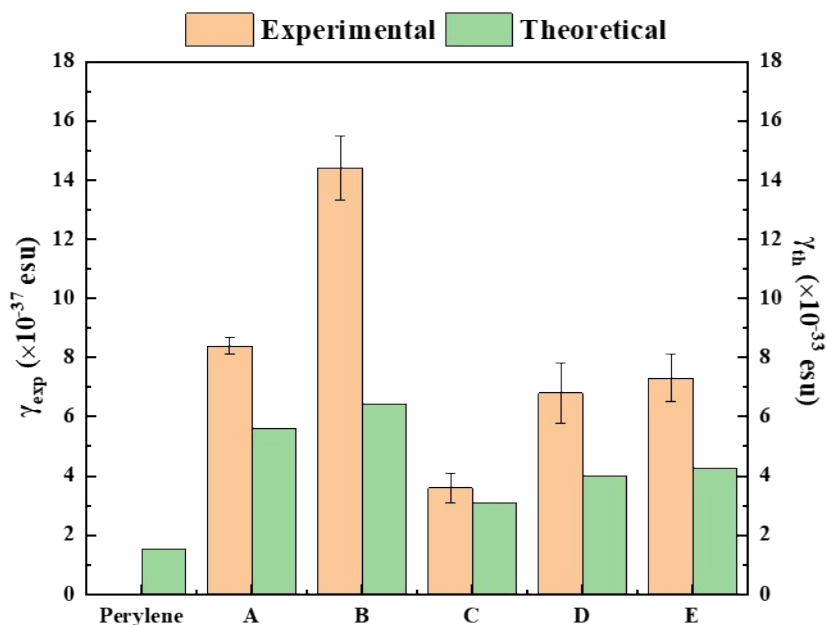


**Figure 10.** Comparison of the experimentally determined (70 fs/800 nm) second hyperpolarizability values of PDI derivatives A-E with the theoretically calculated ones.

From the results summarized in **Table 3**, concerning the different NLO parameters of the PDIs A-E, the following conclusions can be drawn:

(a) For the case of 70 fs, 800 nm laser excitation: all PDI derivatives A-E were found exhibiting similar order of magnitude NLO response (ca. second hyperpolarizability  $\gamma$ , or  $\chi^{(3)}/c$ ), with **B** exhibiting the larger value, followed by **A**, **E** and **D** (in decreasing order), the last two exhibiting very similar  $\chi^{(3)}/c$  and  $\gamma$  values, and **C** exhibiting the lowest response. It is noted that both the experimental results and the theoretical calculations suggest similar trends, concerning the changes of the third-order NLO response between the PDI derivatives studied (see e.g. **Figure 10**). The values of TPA exhibit a similar trend (see also **Table 3**), with PDI **B** exhibiting the larger TPA, with the values for PDIs **A**, **E** and **D** being relatively lower and very similar (within the experimental error) and PDI **C** exhibiting the lowest TPA value. These findings are well aligned with the non-resonant character of the excitation under 800 nm (as no absorption band was observed in the corresponding absorption spectra of the PDIs shown in **Figure 2**).



(b) *Effect of the substitution group:* under non-resonant excitation conditions, i.e., at 800 nm, the *p*-aminoazobenzene functionalized PDIs **A** and **B** exhibited the largest NLO response, followed by the amino and aniline functionalized PDIs **E** and **D**, respectively, in agreement with the results of the theoretical computations. The same trend holds for the NLO response under resonant excitation conditions, i.e., at 400 nm. However, in this case, the differences of the observed NLO response between the different PDIs are relatively more pronounced, as a result of the resonant excitation.

(b) *Effect of the position of substitution:* the bay functionalized PDIs were found to exhibit larger NLO response than those functionalized at the imide position under both resonant and non-resonant excitation conditions. In more detail, under 800 nm excitation, the bay substituted PDIs **B** and **D** were found to exhibit 2-3 times larger NLO response than the imide position substituted counterparts, **A** and **C**, while the theoretical results confirm successfully this trend as well. The TPA cross-sections of the PDIs exhibit also similar behaviour, with the TPA values of the bay-substituted PDIs **B** and **D** determined to be the larger ones, by a factor of about two. Correspondingly, under 400 nm resonant excitation conditions, the *p*-aminoazobenzene functionalized PDIs **A** and **B** were found to exhibit the largest NLO response, most probably due to the near resonant excitation conditions occurring in this case, as a strong absorption band is located close, at ~404 and ~408 nm, respectively (see also **Figure 2**). In fact, the NLO response of PDIs **A** and **B** was found to be about an order of magnitude larger than that of the aniline substituted PDIs **C** and **D**, and 3-5 times larger than that of the amino-substituted PDI **E**. Conversely, PDIs **C** and **D** exhibited the lowest NLO response.

## CONCLUSIONS

In the present work, the NLO response of some newly synthesised PDI derivatives, featuring *p*-aminoazobenzene (PDI derivatives **A** and **B**), aniline (PDI derivatives **C** and **D**) and amine (PDI derivative **E**) groups, at the imide (PDI derivatives **A**, and **C**) and bay (PDI derivatives **B**, **D** and **E**) positions, was investigated both experimentally and theoretically. The functionalization of the perylene core with these electron donating units, allowed to assess the effect of the respective functionalization on their third-order non-linear optical properties. In addition, the effect of the electronic coupling/decoupling of the aromatic substituents of perylene (as e.g., by the addition of the phenyl group at the bay or imide positions) on the



NLO response was also investigated. The results from DFT theoretical computations predicted the changes in the second hyperpolarizability  $\gamma$  of these PDIs, in excellent agreement with the experimentally determined ones, both demonstrating clearly that the addition of *p*-aminoazobenzene and the substitution of the perylene core at the bay position are leading to stronger NLO response under fs laser excitation. Theoretical analysis shows that the observed NLO alterations, between the different PDI derivatives, are attributed to changes on the second hyperpolarizability density, caused by group functionalization at either imide or bay position. This finding is further corroborating by the experimental results and highlights the importance of the structure-property relationship of the PDIs on the efficient tuning of their NLO properties. It is interesting to note that under non-resonant fs excitation, at 800 nm, the NLO refractive response of the PDIs, except that of derivative **A** was insignificant, while under resonant excitation, i.e., 400 nm, the NLO absorptive and refractive response were similarly contributed to the observed NLO response. Under ns laser excitation conditions, where the experimental results cannot be compared with the theoretical predictions, the imide position *p*-aminoazobenzene substituted PDI derivative **A** was found exhibiting the largest NLO response, while the bay substituted PDI derivatives **B** and **D**, and the imide substituted PDI derivative **C** exhibited very similar NLO response.

## ACKNOWLEDGEMENT

AA acknowledges that this work was partially performed under the COST Action CA21101 “Confined molecular systems: from a new generation of materials to the stars” (COSY) supported by COST (European Cooperation in Science and Technology). F.F.-L. thanks Grant PID2022-140315NB-I00 funded by MICIU/AEI/ 10.13039/501100011033 and by ERDF/EU. F.F.-L. is also indebted to the Generalitat Valenciana (CIPROM/ 2021/059) and the Advanced Materials program by MCIN with funding from European Union NextGenerationEU (PRTR-C17.I1) and Generalitat Valenciana (MFA/2022/ 028).



**References**

- 1 F. Würthner, *Chem. Commun.*, 2004, **4**, 1564–1579.
- 2 A. Nowak-Król and F. Würthner, *Org. Chem. Front.*, 2019, **6**, 1272–1318.
- 3 C. Huang, S. Barlow and S. R. Marder, *J. Org. Chem.*, 2011, **76**, 2386–2407.
- 4 C. Li and H. Wonneberger, *Adv. Mater.*, 2012, **24**, 613–636.
- 5 E. Kozma and M. Catellani, *Dyes Pigm.*, 2013, **98**, 160–179.
- 6 M. Guide, S. Pla, A. Sharenko, P. Zalar, F. Fernández Lázaro, Á. Sastre Santos and T.-Q. Nguyen, *Phys. Chem. Chem. Phys.*, 2013, **15**, 18894–18899.
- 7 X. Zhan, J. Zhang, S. Tang, Y. Lin, M. Zhao, J. Yang, H. L. Zhang, Q. Peng, G. Yu and Z. Li, *Chem. Commun.*, 2015, **51**, 7156–7159.
- 8 F. Fernández Lázaro, N. Zink Lorre and Á. Sastre Santos, *J. Mater. Chem. A*, 2016, **4**, 9336–9346.
- 9 N. Zink Lorre, E. Font Sanchis, Á. Sastre Santos and F. Fernández Lázaro, *Chem. Commun.*, 2020, **56**, 3824–3838.
- 10 R. Canton-Vitoria, Y. Matsunaga, S. Zhang, M. Xue, M. Osada, R. Kitaura, *Nanoscale* 2025, **17**, 8084–8100
- 11 I. F. A. Mariz, S. Raja, T. Silva, S. Almeida, E. Torres, C. Baleizão and E. Maçôas, *Dyes Pigm.*, 2021, **193**, 109470.
- 12 W. Hussain, H. S. Ali, M. S. Iqbal, M. R. Bashir, M. A. Khan, M. Hanif, Y. Sandali, A. Irfan and H. Li, *Theor. Chem. Acc.*, 2024, **143**, 27.
- 13 L. Wang, Y. L. Liu, Q. J. Li, S. H. Chen, D. He and M. S. Wang, *J. Phys. Chem. A*, 2022, **126**, 870–878.
- 14 F. A. Jerca, V. V. Jerca and R. Hoogenboom, *Nat. Rev. Chem.*, 2022, **6**, 51–69.
- 15 M. Dudek, A. Kaczmarek-Kędziera, R. Deska, J. Trojnar, P. Jasik, P. Młynarz, M. Samoć and K. Matczyszyn, *J. Phys. Chem. B*, 2022, **126**, 6063–6073.
- 16 E. Piovesan, L. De Boni, E. Ishow and C. R. Mendonça, *Chem. Phys. Lett.*, 2010, **498**, 277–280.
- 17 M. Gascón-Moya, A. Pejoan, M. Izquierdo-Serra, S. Pittolo, G. Cabré, J. Hernando, R. Alibés, P. Gorostiza and F. Busqué, *J. Org. Chem.*, 2015, **80**, 9915–9925.
18. Y. Song, J. Sun, X. He, M. Liao, J. Zhao, W. Zeng, S. Zhou, H. Chen, *Angew. Chem. Int. Ed.* 2023, **62**, e202306418.
19. H. Qin, L. Zhao, L. Zheng, Z. Ma, M. Liao, J. Sun, C. Sun, H. Chen, *Chem. Eur. J.* 2025, **31**, e202403332.





- 20 X. Shang, J. Ahn, J. H. Lee, J. C. Kim, H. Ohtsu, W. Choi, I. Song, S. K. Kwak and J. H. Oh, *ACS Appl. Mater. Interfaces*, 2021, **13**, 12278–12285.
- 21 W. Yue, W. Jiang, M. Böckmann, N. L. Doltsinis and Z. Wang, *Chem. Eur. J.*, 2014, **20**, 5209–5213.
- 22 L. Huang, L. Bin, J. Shen, W. F. Liu, K. Zhou, Y. L. Traskovskis, W. Song, Z. H. Jiang, X. K. Wang and X. K. Ren, *Chem. Commun.*, 2020, **56**, 3123–3126.
- 23 T. Gao, W. F. Zhou, Y. Zhao, L. Shen, W. Y. Chang, R. K. Musendo, E. Q. Chen, Y. L. Song and X. K. Ren, *Chem. Commun.*, 2019, **55**, 3012–3014.
- 24 Y. Yang, Y. Wang, Y. Xie, T. Xiong, Z. Yuan, Y. Zhang, S. Qian and Y. Xiao, *Chem. Commun.*, 2011, **47**, 10749–10751.
- 25 S. L. Oliveira, D. S. Corrêa, L. Misoguti, C. J. L. Constantino, R. F. Aroca, S. C. Zilio and C. R. Mendonça, *Adv. Mater.*, 2005, **17**, 1890–1893.
- 26 M. Younis, J. Long, S. Q. Peng, X. S. Wang, C. Chai, N. Bogliotti and M. H. Huang, *J. Phys. Chem. Lett.*, 2021, **12**, 3655–3661.
- 27 Q. Yan and D. Zhao, *Org. Lett.*, 2009, **11**, 3426–3429.
- 28 P. Yan, M. W. Holman, P. Robustelli, A. Chowdhury, F. I. Ishak and D. M. Adams, *J. Phys. Chem. B*, 2005, **109**, 130–137.
- 29 M. Barrejón, S. Pla, I. Berlanga, M. J. Gómez-Escalonilla, L. Martín-Gomis, J. L. G. Fierro, M. Zhang, M. Yudasaka, S. Iijima, H. B. Gobeze, F. D'Souza, Á. Sastre-Santos and F. Langa, *J. Mater. Chem. C*, 2015, **3**, 4960–4969.
- 30 H. Langhals and S. Kirner, *Eur. J. Org. Chem.*, 2000, **2**, 365–380.
- 31 P. Aloukos, K. Iliopoulos, S. Couris, D. M. Guldi, C. Sooambar, A. Mateo-Alonso, P. G. Nagaswaran, D. Bonifazi and M. Prato, *J. Mater. Chem.*, 2011, **21**, 2524–2534.
- 32 N. Karampitsos, D. Kyrginas, and S. Couris, *Opt. Lett.*, 2020, **45**, 1814–1817.
- 33 S. Vajiravelu, L. Ramunas, G. Juozas Vidas, G. Valentas, J. Vygintas and S. Valiyaveetil, *J. Mater. Chem.*, 2009, **19**, 4268–4275.
- 34 A. Dreuw and M. Head-Gordon, *Chem. Rev.*, 2005, **105**, 4009–4037.
- 35 D. Jacquemin, E. A. Perpète, G. E. Scuseria, I. Ciofini and C. Adamo, *J. Chem. Theory Comput.*, 2008, **4**, 123–135.
- 36 D. Jacquemin, A. Planchat, C. Adamo and B. Mennucci, *J. Chem. Theory Comput.*, 2012, **8**, 2359–2372.
- 37 B. Mennucci and J. Tomasi, *J. Chem. Phys.*, 1997, **106**, 5151–5158.





- 732 38 M. J. Frisch, G. W. Trucks, H. B. Schlegel, G. E. Scuseria, M. A. Robb, J. R. Cheeseman,  
733 G. Scalmani, V. Barone, G. A. Petersson, H. Nakatsuji et al., Gaussian 16 Rev. B.01,  
734 Gaussian Inc., Wallingford, CT, USA, 2016.
- 735 39 M. Stavrou, N. Chazapis, E. Nikoli, R. Arenal, N. Tagmatarchis and S. Couris, ACS Appl.  
736 Nano Mater., 2022, **5**, 16674–16686.
- 737 40 M. Stavrou, I. Papadakis, T. I. Narayanan and S. Couris, J. Phys. Chem. C, 2021, **125**,  
738 16075–16085.
- 739 41 M. Stavrou, N. Chazapis, V. Georgakilas and S. Couris, Chem. Eur. J., 2023, **29**.
- 740 42 H. D. Cohen and C. C. Roothaan, J. Chem. Phys., 1965, **43**, S34–S39.
- 741 43 H. Rutishauser, Numer. Math., 1963, **5**, 48–54.
- 742 44 W. Romberg, K. Nor. Vidensk. Selsk. Forsk., 1955, **28**, 30–36.
- 743 45 T. Yanai, D. P. Tew and N. C. Handy, Chem. Phys. Lett., 2004, **393**, 51–57.
- 744 46 T. Miletić, A. Fermi, I. Papadakis, I. Orfanos, N. Karampitsos, A. Avramopoulos, N.  
745 Demitri, F. De Leo, S. J. A. Pope, M. G. Papadopoulos, S. Couris and D. Bonifazi, Helv.  
746 Chim. Acta, 2017, 100.
- 747 47 Y. Zhao and D. G. Truhlar, Theor. Chem. Acc., 2008, **120**, 215–241.
- 748 48 D. Jacquemin, A. Femenias, H. Chermette, I. Ciofini, C. Adamo, J.-M. André and E. A.  
749 Perpète, J. Phys. Chem. A, 2006, **110**, 5952–5959.
- 750 49 K. Aidas, C. Angeli, K.L. Bak, V. Bakken, R. Bast, L. Boman, O. Christiansen, R.  
751 Cimiraglia, S. Coriani, P. Dahle, et al., The Dalton quantum chemistry program system.  
752 WIREs Comput. Mol. Sci., 2014, **4**, 269–284.
- 753 50 T. Lu, *J. Chem. Phys.*, 2024, **161**, 082503.
- 754 51 S. Gámez-Valenzuela, I. Torres-Moya, A. Sánchez, B. Donoso, J. T. López Navarrete, M.  
755 C. Ruiz Delgado, P. Prieto and R. Ponce Ortiz, Chem. Eur. J., 2023, **29**, e202301639.
- 756 52 A. Keerthi and S. Valiyaveetil, J. Phys. Chem. B, 2012, **116**, 4603–4614.
- 757 53 G. He, Nonlinear Optics and Photonics, Oxford University Press, Oxford, 2015.
- 758 54 Y. Yang, F-H Wang, Y-S Zhou, L. Yuan, J. Yang, Phys. Rev. A, 2005, **71**, 013202
- 759 55 N. Matsuzawa and D. A. Dixon, J. Phys. Chem, 1992, **96**, 6872–6875.
- 760



The data supporting this article have been included as part of the Supplementary Information.

[View Article Online](#)  
DOI: 10.1039/D5MA01344E

